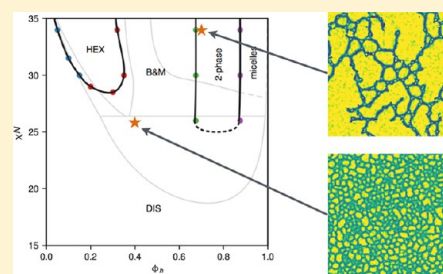


Field-Theoretic Simulations of Fluctuation-Stabilized Aperiodic “Bricks-and-Mortar” Mesophase in Miktoarm Star Block Copolymer/Homopolymer Blends

Yi-Xin Liu,^{†,‡} Kris T. Delaney,[‡] and Glenn H. Fredrickson^{*,‡,§}[†]State Key Laboratory of Molecular Engineering of Polymers, Department of Macromolecular Science, Fudan University, Shanghai 200433, China[‡]Materials Research Laboratory and [§]Department of Materials and Department of Chemical Engineering, University of California, Santa Barbara, Santa Barbara, California 93106, United States

ABSTRACT: A new class of thermoplastic elastomers possessing unusual mechanical properties has recently been discovered in binary blends of A-*b*-(B-*b*-A')_n miktoarm star block copolymers and A homopolymers that spontaneously form an unusual, thermodynamically stable, aperiodic “bricks-and-mortar” (B&M) mesophase morphology. The B&M mesophase is believed to be stabilized by thermal fluctuations as in the well-known case of the bicontinuous microemulsion phase. Here, two-dimensional field-theoretic simulations are used to study the equilibrium self-assembly of such miktoarm polymer binary blends. As expected, the B&M mesophase is not present in the mean-field phase diagram obtained with self-consistent field theory, but complex Langevin (CL) simulations, which fully incorporate thermal fluctuation effects, reveal dramatic changes to the phase diagram. A region of strong fluctuations results in the emergent stabilization of the B&M mesophase in a broad composition channel positioned between microphase separation and macrophase separation envelopes, consistent with experimental observations. Our simulations clarify the topology of the blend phase diagram and suggest that the B&M mesophase, at least as observed near the order–disorder transition, has no long-range or quasi-long-range positional or orientational order.



INTRODUCTION

In the past two decades, mean-field theories have achieved remarkable successes in predicting the equilibrium phases of block copolymers and their alloys with homopolymers.^{1–5} In particular, self-consistent field theory (SCFT) has been used extensively to compute morphologies of ordered mesophases, order–disorder transitions (ODT), and order–order transitions (OOT) and to construct phase diagrams.^{6–15} However, the validity of SCFT is restricted to concentrated solutions or melts of high-molecular-weight polymers far from critical phase transitions.¹⁶ Close to such phase transitions, it has been demonstrated, for example in polyisoprene–polystyrene diblock copolymers, that SCFT-computed phase diagrams are inaccurate: block copolymer ODT boundaries are shifted to lower temperatures (higher Flory–Huggins interaction parameter χN), and the contours of phase boundaries are significantly distorted.¹⁷ These are largely quantitative corrections, except close to the strictly symmetric case where the disorder-to-lamellar transition is changed by fluctuations from second-order to first-order character, breaking the critical point.^{18,19} This is an example where the mean-field approach fails in a more significant “qualitative” way because fluctuation effects become strong enough to alter the topology of the phase diagram.

The bicontinuous microemulsion (B μ E) observed in a ternary diblock copolymer–homopolymer blend (A-*b*-B/A/B) is a second example of a qualitative failure of mean-field theory.^{20–22}

Unlike conventional inhomogeneous phases of block copoly-

mers, such as the lamellar phase (LAM) and the hexagonal cylinder phase (HEX), the B μ E lacks long-range positional and orientational order: the A-rich and B-rich domains are separated by undulating interfaces of almost zero mean curvature, with the individual A and B domains forming continuous random networks. It has been found that the B μ E phase appears in a narrow channel near the mean-field Lifshitz critical point (LP), which is destroyed by fluctuations. This B μ E mesophase has been extensively studied experimentally^{20–22} and theoretically.^{23–31} Among theoretical approaches, Duchs et al.³¹ demonstrated that field-theoretic simulations with complex Langevin (CL) sampling is a powerful approach for identifying the B μ E channel in the phase diagram and examining the role of fluctuations in stabilizing the aperiodic B μ E morphology.

The CL method was originally developed to solve lattice gauge theories³² with complex actions³³ and was introduced to polymer field theory by Ganesan and Fredrickson.^{34,35} The method incorporates fluctuation effects by introducing a Langevin dynamics to sample complex-valued field configurations. Thermodynamic observables are then obtained by averaging a corresponding operator over the generated field configurations. The method has proven to be broadly applicable for studying fluctuation phenomena in polymeric assemblies, for example in

Received: May 29, 2017

Revised: July 10, 2017

polymer solutions,^{36,37} melts of block copolymers and polymer blends,^{31,35,38} polymer nanocomposites,^{39,40} and polyelectrolytes.^{41–43} Meanwhile, the method has been advanced by new algorithms that significantly improve stability, accuracy, and efficiency^{44–46} as well as the range of accessible systems⁴⁷ and expand the sampling methods available for mapping phase diagrams.^{38,48,49}

Recently, Shi et al.⁵⁰ reported a new aperiodic inhomogeneous phase, which they designated the “bricks-and-mortar” mesophase (B&M), in a binary blend of S-*b*-(I-*b*-S')₃ miktoarm star block copolymer with polystyrene homopolymer. Here, S and S' denote blocks of polystyrene of different lengths, and I denotes polyisoprene; each miktoarm star block copolymer consists of one long polystyrene arm joined to three polyisoprene-*b*-polystyrene arms at the polyisoprene ends.⁵¹ Blending with homopolystyrene yields the B&M mesophase, which exhibits a nanocellular morphology with apparently discrete polystyrene-rich domains (“bricks”) well dispersed within a continuous polyisoprene-rich matrix (“mortar”). This cellular nanomaterial combines high modulus from the discrete polystyrene-rich phase with recoverable elasticity from the continuous rubbery polyisoprene-rich matrix. A key design parameter in the miktoarm polymers is the ratio $\tau = N_S/(N_S + N_{S'})$, where N_S and $N_{S'}$ denote the degrees of polymerization of the long S arm and the shorter S' peripheral blocks. When τ is tuned to the range of 0.85–0.95,⁵¹ the combination of the asymmetric S–I₃ junction and the S/S' block polydispersity conspire to drive interfaces to curve strongly toward polystyrene. As a result, the discrete phase can accommodate an extremely high volume fraction of polystyrene, rendering the new material hard, yet elastic and tough. This material thus offers unique mechanical properties, distinguishing it from traditional thermoplastic elastomers (TPEs) which are elastic but comparatively soft.

The B&M mesophase shares some common features with the B μ E phase: it is structured but disordered and emerges in the region of composition between microphase separation and macrophase separation. It is believed that it is also stabilized by fluctuations.⁵⁰ However, as a new discovery, the B&M mesophase is much less well understood than the B μ E phase, and theoretical insight is needed to guide the design and optimization of these novel nanocellular materials and TPEs.

In this work we employ two-dimensional CL simulations to study the phase behavior of a binary blend of miktoarm star block copolymers and homopolymers. A mean-field phase diagram is first constructed via SCFT to guide the search for the B&M mesophase. It is subsequently found that the LAM/HEX coexistence region in the mean-field phase diagram is destroyed by strong composition fluctuations, resulting in the stabilization of the B&M mesophase. The B&M mesophase is also observed to encroach on the HEX- and LAM-phase regions neighboring the LAM/HEX coexistence channel. Indeed, for the specific blend investigated, a stable LAM phase is not observed; in its place is a region of coexistence (macrophase separation) between B&M and a micellar phase dilute in mikto-polymer.

THEORETICAL FORMULATION

Molecularly Informed Field Theory Model. We consider a binary blend consisting of n_c A₁-(B-*b*-A₂)₃ miktoarm star polymers and n_h A homopolymers in a volume V . The miktoarm polymer has one arm (A₁) consisting of A monomers joined to three identical diblock arms (B-*b*-A₂) at the B block ends (see Figure 1). We assume equal statistical segment lengths, b , for both A and B monomers and they occupy the same volume v_0 ,

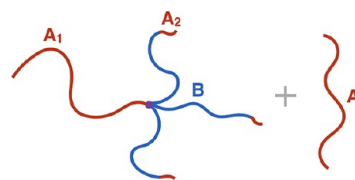


Figure 1. Schematic illustration of the architecture of the miktoarm star block copolymer, A₁-(B-*b*-A₂)₃, in a binary blend with A homopolymer.

which defines an average monomer number density $\rho_0 = v_0^{-1}$ in the incompressible limit. The fractional lengths of A₁ and A₂ blocks can be defined as $f_1 = N_{A_1}/N$ and $f_2 = N_{A_2}/N$, respectively, where $N = N_{A_1} + 3(N_B + N_{A_2})$ is the total number of monomers in a miktoarm polymer and N_K represents the number of monomers comprising the K th block. The molecular asymmetry parameter τ used in ref 51 is thus $\tau = f_1/(f_1 + f_2)$, while the overall volume fraction of A-type monomers on the miktopolymer is $f = f_1 + 3f_2$. The length of each B block relative to N is given by $(1 - f)/3$, and we define the length of the homopolymer relative to N to be α . The composition of the homopolymer in the blend is $\phi_h = n_h \alpha N / N_t$, where $N_t = n_c N + n_h \alpha N$ is the total number of segments from all chains in the volume V .

We derive the field-theory model for such a binary blend closely following the procedure presented in the monograph by Fredrickson.⁴ More recent advances in models for field-theoretic simulations have yielded an understanding of how to avoid UV divergences and stability difficulties in sampling the field theory by redefining the model to contain no pathological or singular features. We follow the same approach as Delaney and Fredrickson³⁸ in smearing the particle centers by convolving with a normalized Gaussian function^{46,52} of width a , which is equivalent to replacing contact interactions with soft Gaussian potentials, and admitting a small but finite compressibility to the melt. This type of model has been shown³⁸ to offer significant improvements in CL sampling stability and to make predictions of phase boundaries, in quantitative agreement with soft-potential particle simulations. However, as a consequence of the smearing procedure, the χN parameter, while playing the traditional role of controlling phase separation, is renormalized and should not be interpreted as the χN that appears in Leibler's RPA.³⁸

The canonical partition function of our smeared, weakly compressible melt model can be written as

$$\mathcal{Z}_c = \frac{1}{\lambda_T^{3N_t} n_c! n_h!} \int \prod_{i=1}^n \mathcal{D}\mathbf{r}_i \exp(-U_0 - U_1 - U_2) \quad (1)$$

where $n = n_c + n_h$ is the total number of polymer chains and \mathbf{r}_i denotes the conformation of the i th polymer chain. Note that all energies are scaled by $k_B T$, where k_B is the Boltzmann constant and T is the temperature.

The configuration of the ν arm of miktopolymer molecule $i \in [1, n_c]$ is described by a continuous space curve $\mathbf{r}_i^\nu(s)$, where the contour parameter $s \in [0, N_\nu]$ is measured from the free end of the ν arm. Similarly, the configuration of the homopolymer chain of index $i \in [1, n_h]$ is described by $\mathbf{r}_i^h(s)$ with $s \in [0, \alpha N]$. The energetic contribution due to bond linkage for a continuous Gaussian chain model is given by

$$U_0 = \frac{3}{2b^2} \sum_{i=1}^{n_c} \sum_{\nu} \int_0^{N_\nu} ds \left| \frac{d\mathbf{r}_i^\nu(s)}{ds} \right|^2 + \frac{3}{2b^2} \sum_{i=1}^{n_h} \int_0^{\alpha N} ds \left| \frac{d\mathbf{r}_i^h(s)}{ds} \right|^2 \quad (2)$$

The energy arising from the interaction between A and B monomers is modeled by a modified Flory–Huggins interaction of strength, χ

$$U_1 = v_0 \chi \int d\mathbf{r} \check{\rho}_A(\mathbf{r}) \check{\rho}_B(\mathbf{r}) \quad (3)$$

The microscopic monomer densities are

$$\hat{\rho}_A(\mathbf{r}) = \sum_{i=1}^{n_c} \sum_{\nu} \int_{\Omega_A} ds \delta(\mathbf{r} - \mathbf{r}_i^{\nu}(s)) + \sum_{i=1}^{n_h} \int_0^{\alpha N} ds \delta(\mathbf{r} - \mathbf{r}_i^h(s)) \quad (4)$$

$$\hat{\rho}_B(\mathbf{r}) = \sum_{i=1}^{n_c} \sum_{\nu} \int_{\Omega_B} ds \delta(\mathbf{r} - \mathbf{r}_i^{\nu}(s)) \quad (5)$$

where Ω_K includes all contour positions of K -species blocks, and the smeared density operators are then obtained by convolving $\hat{\rho}_K$ with $\Gamma(\mathbf{r}; a) = (2\pi a^2)^{-3/2} \exp(-r^2/2a^2)$: $\check{\rho}_K(\mathbf{r}) = (\Gamma^* \hat{\rho}_K)(\mathbf{r})$. The final energetic contribution, U_2 , is a Helfand potential

$$U_2 = \frac{v_0 \zeta}{2} \int d\mathbf{r} [\check{\rho}_A(\mathbf{r}) + \check{\rho}_B(\mathbf{r}) - \rho_0]^2 \quad (6)$$

which allows local deviations of the total density from ρ_0 with extent controlled by the Helfand compressibility coefficient ζ .

Performing Hubbard–Stratonovich transformations on the partition function in eq 1 requires introduction of two auxiliary fields and leads to a field theory

$$\mathcal{Z}_c = \mathcal{Z}_0 \int \mathcal{D}w_+ \int \mathcal{D}w_- \exp(-H[w_+, w_-]) \quad (7)$$

$$\begin{aligned} H[w_+, w_-] = & \frac{C}{\chi N + 2\zeta N} \int d\mathbf{r} [w_+(\mathbf{r})^2 - 2i\zeta N w_+(\mathbf{r})] \\ & + \frac{C}{\chi N} \int d\mathbf{r} w_-(\mathbf{r})^2 - n_c \ln Q_c[\Gamma^* w_A, \Gamma^* w_B] - n_h \\ & \ln Q_h[\Gamma^* w_A] \end{aligned} \quad (8)$$

where the coefficient \mathcal{Z}_0 contains the contribution from an equivalent ideal gas of miktoarm and homopolymer continuous Gaussian chains, an energy shift from completing the square of the interaction terms, and Gaussian denominators of the auxiliary fields.³⁸ $C = \rho_0 R_g^3/N$ is the dimensionless chain number density, acting as a Ginzburg parameter, which scales the Hamiltonian and controls the relative importance of composition fluctuations,⁴ $R_g = b\sqrt{N/6}$ is the radius gyration of a reference linear chain of length N , and all spatial coordinates \mathbf{r} and the volume V have been scaled to units of R_g and R_g^3 . The fields $w_A = iw_+ - w_-$ and $w_B = iw_+ + w_-$ are conjugate to $\check{\rho}_A$ and $\check{\rho}_B$, respectively.

The normalized single-molecule partition function of miktoarm polymers, Q_c , can be evaluated as

$$Q_c[\Gamma^* w_A, \Gamma^* w_B] = \frac{1}{V} \int d\mathbf{r} \prod_{\nu} q_{\nu}(\mathbf{r}, s = N_{\nu}) \quad (9)$$

where the propagators $q_{\nu}(\mathbf{r}, s)$ describe the probability of finding a monomer indexed by s at position \mathbf{r} by propagating from the free end of arm ν . These propagators satisfy the following Fokker–Planck equations

$$\partial_s q_{\nu}(\mathbf{r}, s) = \left[\frac{b}{6} \nabla^2 - \Gamma^* w_{\nu}(\mathbf{r}; s)/N \right] q_{\nu}(\mathbf{r}, s) \quad (10)$$

subject to initial conditions $q_{\nu}(\mathbf{r}, 0) = 1$ and $w_{\nu}(\mathbf{r}; s) = w_A(\mathbf{r})$ for $s \in \Omega_A$ and $w_{\nu}(\mathbf{r}; s) = w_B(\mathbf{r})$ otherwise. Similarly, the normalized

single-molecule partition function of homopolymer chains is given by

$$Q_h[\Gamma^* w_A] = \frac{1}{V} \int d\mathbf{r} q_h(\mathbf{r}, s = \alpha N) \quad (11)$$

where the propagator q_h also satisfies eq 10 with the field w_A .

Backward propagators, q^{\dagger} , initiated from the junction of the star polymer and from the $s = \alpha N$ end of the homopolymer are required to evaluate A and B monomer densities. These propagators also satisfy eq 10, but for the miktoarm polymer are subject to different initial conditions reflecting the tethering constraint at the star junction: $q_{\nu}^{\dagger}(\mathbf{r}, 0) = \prod_{\mu \neq \nu} q_{\mu}(\mathbf{r}, s = N_{\mu})$. The homopolymer, which is free at both ends, retains the initial condition $q_h^{\dagger}(\mathbf{r}, 0) = 1$ for the backward propagator.

After solving the MDEs, fractional monomer densities $\phi_K = \check{\rho}_K/\rho_0$ are readily obtained using

$$\begin{aligned} \phi_A(\mathbf{r}) = & \Gamma^* \left[\frac{1 - \phi_h}{NQ_c} \sum_{\nu} \int_{\Omega_A} ds q_{\nu}(\mathbf{r}, s) q_{\nu}^{\dagger}(\mathbf{r}, N_{\nu} - s) \right] \\ & + \Gamma^* \left[\frac{\phi_h}{\alpha N Q_h} \int_0^{\alpha N} ds q_h(\mathbf{r}, s) q_h^{\dagger}(\mathbf{r}, \alpha N - s) \right] \end{aligned} \quad (12)$$

$$\phi_B(\mathbf{r}) = \Gamma^* \left[\frac{1 - \phi_h}{NQ_c} \sum_{\nu} \int_{\Omega_B} ds q_{\nu}(\mathbf{r}, s) q_{\nu}^{\dagger}(\mathbf{r}, N_{\nu} - s) \right] \quad (13)$$

These density operators must be averaged over w_A and w_B field fluctuations to obtain physical densities.

Self-Consistent Field Theory. Mean-field theory can be obtained by performing a saddle point approximation to the integral in eq 7. Under this approximation, the free energy of the system is determined by configurations of w_+ and w_- fields at the saddle point

$$F = H[w_+^*, w_-^*] \quad (14)$$

The saddle point configurations w_+^* and w_-^* are found by solving the following nonlinear equations

$$iw_+^* = \frac{1}{2} \chi N (\phi_A + \phi_B) + \zeta N (\phi_A + \phi_B - 1) \quad (15)$$

$$w_-^* = \frac{1}{2} \chi N (\phi_A - \phi_B) \quad (16)$$

where the densities ϕ_A and ϕ_B can be viewed as implicit functionals of w_+^* and w_-^* through the modified diffusion equation, eq 10.

Equations 10, 12, 13, 15, and 16 form a complete set of self-consistent field equations which we solve numerically on a uniform spatial collocation mesh with periodic boundary conditions. Equations 15 and 16 are relaxed by a semi-implicit Seidel (SIS) algorithm,⁵³ while the Fokker–Planck equations (eq 10) are solved by a pseudospectral second-order operator splitting algorithm.^{54,55}

For all calculations presented here, we set the compressibility coefficient to $\zeta N = 100$, implying a weakly compressible melt, and the smearing constant as $a = 0.2R_g$. The spatial collocation grid spacing is no larger than $0.2R_g$, which we determined is sufficient to fully resolve the structures and thermodynamic properties of interest, and the contour step Δs is fixed at 0.005.

Complex Langevin Simulations. Complex Langevin (CL) simulations have been performed to obtain approximation-free

solutions to the molecular field theory model. In the CL technique, a sequence of configurations of the auxiliary fields are generated by means of the following Langevin dynamics³⁸

$$\partial_t w_i(\mathbf{r}, t) = -\lambda_i \frac{\delta H[\{w_i\}]}{\delta w_i(\mathbf{r}, t)} + \eta_i(\mathbf{r}, t) \quad (17)$$

where $\eta_i(\mathbf{r}, t)$ is a Gaussian noise obeying the fluctuation–dissipation theorem: $\langle \eta_i(\mathbf{r}, t) \rangle = 0$ and $\langle \eta_i(\mathbf{r}, t) \eta_i(\mathbf{r}', t') \rangle = 2\lambda_i \delta(\mathbf{r} - \mathbf{r}') \delta(t - t')$. Any thermodynamic observable O is obtained from an average of generated samples of a corresponding field-based operator \hat{O} : $O = \frac{\Delta t}{T} \sum_{j=1}^{N_T} \hat{O}[\{w_i^{(j\Delta t)}\}]$ where the total simulation time is $T = N_T \Delta t$. The spatial and contour resolutions used are the same as for SCFT.

We adopt an exponential time differencing with predictor–corrector (ETDPEC) scheme⁴⁷ to integrate the Langevin equations, which significantly improves the stability and accuracy over simpler algorithms. All CL simulations were performed at an intermediate fluctuation strength with dimensionless chain number density $C = 20$ ($\bar{N} = b^6 v_0^{-2} N \approx 10\,000$). Note that this value for C is larger than the most appropriate value for experimental correspondence ($C \approx 7$); the resultant weakening of field fluctuations greatly enhanced stability of the CL time stepper. The concomitant gain in sampling efficiency allows for much larger simulation cells and longer annealing cycles than would otherwise be attainable. We expect qualitative changes of the phase diagram induced by fluctuation corrections to manifest also at this higher C value. After equilibration, a total of 5×10^5 samples were collected for each evaluation of the thermodynamic observable, unless otherwise stated. For all CL simulations, Δt is set to 0.002, and the calculations are conducted in two-dimensional (2D) space. The reduction in dimensionality allows us to conduct CL simulations with unprecedented cell sizes of up to $110R_g$ on a side or approximately $1.5\ \mu\text{m}$ for the comparable experimental system. This has the benefit of providing access to the microscopy-relevant scales in experiment, but obviously our results should be interpreted cautiously, as fluctuation-induced phenomena in 3D could potentially have a different character than in 2D.

RESULTS AND DISCUSSION

In the following simulations, we choose $f_1 = 0.28$, $f_2 = 0.04$, and $\alpha = 0.14$, roughly corresponding to the experimental case of $M_n(\text{PS}) = 80.5\ \text{kg/mol}$, $M_n(\text{PS}') = 11.0\ \text{kg/mol}$, $M_n(\text{PI}) = 56.0\ \text{kg/mol}$, and $M_n(\text{hPS}) = 44.6\ \text{kg/mol}$.⁵⁰ The experimental results of Shi et al.⁵⁰ suggest that this particular molecular architecture gives the widest range of homopolymer volume fraction for observing the B&M mesophase.

Mean-Field Phase Diagram. The mean-field phase diagram shown in Figure 2 was obtained by comparing free energies of various phases computed by SCFT calculations. Inspired by the experimental observations, only the lamellar (LAM), hexagonally packed cylinders (HEX), and disordered (DIS) phases, and their coexistences, were considered in constructing the phase diagram. The mean-field phase diagram has a large two-phase region bounded by DIS–DIS, HEX–DIS, and HEX–LAM coexistence lines. The HEX- and LAM-phase regions expand rapidly as χN increases from 25 to 35. Note that the maximum segregation strength in the computed phase diagram ($\chi N = 35$) is significantly weaker than the experimental segregation strength ($\chi N = 270$),⁵⁰ for reasons both of computational practicality and to reveal the ODT envelope. With increasing ϕ_h , homopolymers tend to aggregate in the A-rich domains of the ordered structures,

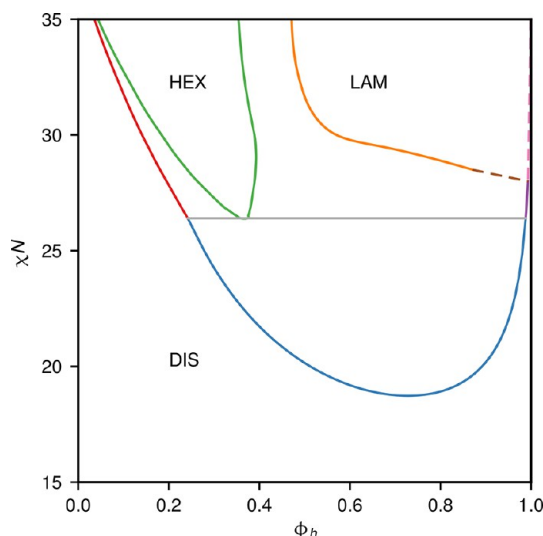


Figure 2. Mean-field phase diagram of the miktoarm polymer binary blend. HEX, LAM, and DIS one-phase pockets are separated by large HEX–DIS, HEX–LAM, and DIS–DIS two-phase coexistence regions. Dashed lines are inferred phase boundaries.

swelling those domains significantly. As $\phi_h \rightarrow 1$, it becomes challenging to resolve the highly swollen domains and to guarantee no unbinding transition. The dashed lines at the top right corner of the phase diagram are HEX–LAM and LAM–DIS coexistence lines inferred from the more reliable region. It is known that the stability of the highly swollen LAM phase is a consequence of the mean-field approximation.⁵⁶ With thermal fluctuations, the swollen LAM phase will eventually become unstable as ϕ_h increases and disorder into a micellar region prior to the SCFT unbinding transition. In addition, a micelle/LAM coexistence region may exist because the order–disorder transition between micellar and LAM phases is first order. Finally, we emphasize that all the DIS phases obtained from SCFT calculations are structureless on all scales, i.e., homogeneous phases. Thus, there is no possibility of capturing a structured disordered phase like B&M mesophase within the confines of SCFT.

As just explained, the B&M mesophase cannot appear in the mean-field phase diagram. However, in the LAM/HEX coexistence region the free energies of the LAM phase and the HEX phase are very close, possessing differences in free energy per chain that differ by about $10^{-4} k_B T$, indicating that these phases compete intensely and consequently are vulnerable to thermal fluctuations. On the basis of these SCFT findings and the experimental phase diagram, we expect thermal fluctuations will destroy the long-range positional order of the ordered structures in the HEX–LAM coexistence channel and consume at least part of the adjacent LAM phase region to form the B&M mesophase. By further increasing the homopolymer volume fraction (e.g., $\phi_h \gtrsim 0.8$), the B&M mesophase should be swollen by homopolymers and eventually become unstable. In this region, the experiments observed the coexistence of B&M and a structured DIS micelle phase, followed by pure micelles for yet larger ϕ_h .

Emergence of the B&M Mesophase. In experiments,⁵⁰ the B&M mesophase appears in a wide range of homopolymer volume fractions from 0.1 to 0.7. This suggests that the B&M mesophase displaces the mean-field HEX–LAM coexistence region shown in Figure 2. To test this hypothesis, we initially conducted two representative two-dimensional large-cell CL

simulations for the miktoarm polymer binary blend with $\phi_h = 0.4$, $\chi N = 26$ (mean-field DIS/DIS coexistence) and $\phi_h = 0.7$, $\chi N = 34$ (mean-field LAM phase). The simulation for $\phi_h = 0.4$ was initialized with a randomly generated field configuration, while the $\phi_h = 0.7$ simulation was initiated with perfect lamellar structures obtained from SCFT calculations. The instantaneous snapshots of the A-segment density distributions from the CL simulations together with the corresponding experimental TEM images are presented in Figure 3. According to Shi et al.,⁵⁰ the

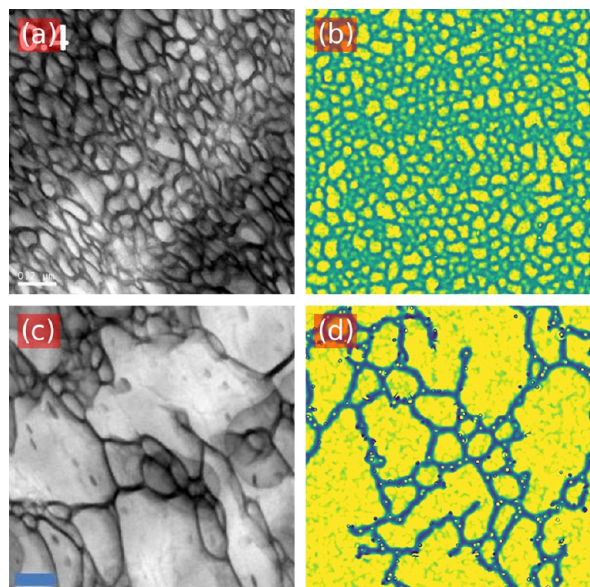


Figure 3. B&M mesophase in the miktoarm polymer binary blend as observed by (a, c) TEM experiments and (b, d) CL simulations. Homopolymer volume fractions are 0.4 and 0.7 for top row and bottom row, respectively. The discrete, bright domains are A-rich (PS-rich) domains for both experimental and simulated results. The scale bars for the experimental images are 200 nm. The sizes of the (b) and (d) images are $110 \times 110 R_g$ and $65.5 \times 65.5 R_g$, respectively. Note that R_g is estimated to be about 15 nm for the experimental miktoarm polymers. Images (a) and (c) are adapted with permission from ref 50.

morphologies for $\phi_h = 0.4$ and $\phi_h = 0.7$ observed with TEM in experiments were designated as the B&M mesophase and a mixture of the B&M mesophase and a PS-rich homogeneous phase, respectively. The simulated morphologies for both conditions resemble the experimental results remarkably well, indicating the importance of a proper treatment of fluctuations and that CL simulations can indeed be used to study the B&M mesophase. It is important to note that large-cell simulations have to be performed to reveal the B&M mesophase because a large field of view (uninfluenced by the periodic boundary conditions) is necessary to reveal its aperiodic nature. Unlike the experimental B&M morphology, however, no evidence of quasi long-range orientational order has been observed in the B&M structures obtained by simulations.

To further examine the structure of the B&M mesophase, we have plotted the density distributions of each block of the miktoarm polymer as well as the homopolymer in Figure 4. Note that specifically for the production of these illustrations, the instantaneous CL-generated morphologies were relaxed to an SCFT saddle point configuration after formation and equilibration, indicating that the B&M structures represent metastable states of the mean-field free energy landscape. It should be noted that the mean-field free energy of such a metastable B&M state as

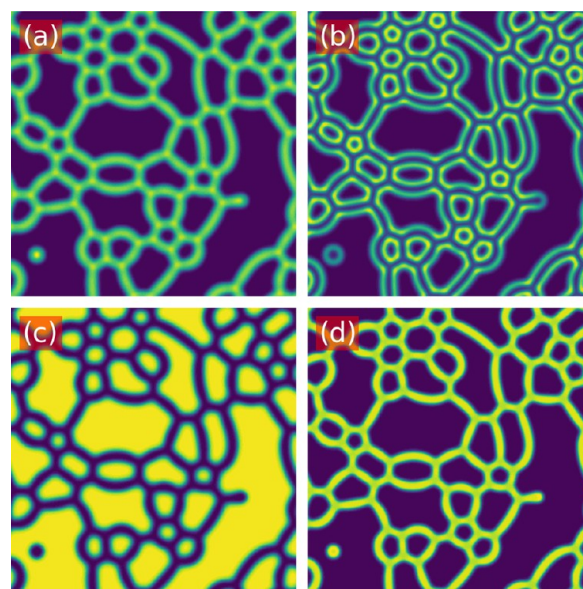


Figure 4. Density distributions of (a) A_2 blocks, (b) A_1 blocks, (c) homopolymers, and (d) B blocks in the miktoarm polymer binary blend as calculated by SCFT initiated from auxiliary fields obtained by equilibrated CL simulations for $\phi_h = 0.6$ at $\chi N = 34$. The field errors are converged to 10^{-4} . The size of each simulation cell is $61.5 \times 61.5 R_g$.

computed by SCFT relaxation is higher than the free energy of the corresponding stable phase shown in the mean-field phase diagram. This procedure removes high-spatial-frequency noise and the imaginary parts of the density operators for easier interpretation of the corresponding image.

In the binary blend we consider here, the length of the homopolymer is smaller than the A_1 block of the miktoarm polymer and longer than the A_2 block. Figure 4a shows that the short A_2 blocks distribute predominantly inside or adjacent to the B-rich domains. This observation confirms the proposition of Shi et al.⁵⁰ that the short A_2 blocks act as a dry brush and resist penetration by the A homopolymer, although not in a conventional dry brush sense since the A_2 blocks largely retreat into the B domains. This observation is also consistent with previous SCFT calculations of ABA' triblock copolymers⁵⁷ and neat miktoarm polymers.⁵¹ The spatial distributions determined by SCFT indicate that the increase of unfavorable contacts of A- and B-monomers is favorable compared to the entropic cost incurred by stretching to distribute short A_2 blocks away from the B domains. A similar phenomenon has been previously observed in the morphologies of a binary blend of Styrolux and polystyrene (PS) homopolymers.⁵⁸ Styrolux is on average a miktoarm star copolymer with four arms. All four arms consist of butadiene-styrene diblocks with a tapered block transition, one of which has a much longer PS block. Therefore, the architecture of Styrolux possesses some similarity with our miktoarm polymer.

Figure 4b reveals that the long A_1 blocks mostly distribute near the periphery of the B-rich domains especially in the vicinity of junctions of the network of the B-rich domains. Thus, the long A_2 blocks are well penetrated by and serve as wet brushes for the added homopolymers. Figure 4c shows that the discrete A-rich domains are filled mainly by the homopolymers, as expected by the connectivity of the miktoarm blocks. In addition, the homopolymers do not penetrate into the B-rich domains; the enthalpic penalty would be too great compared to the small entropy loss for localization. Consequently, we can expect further addition of homopolymer will continue to swell the A-rich

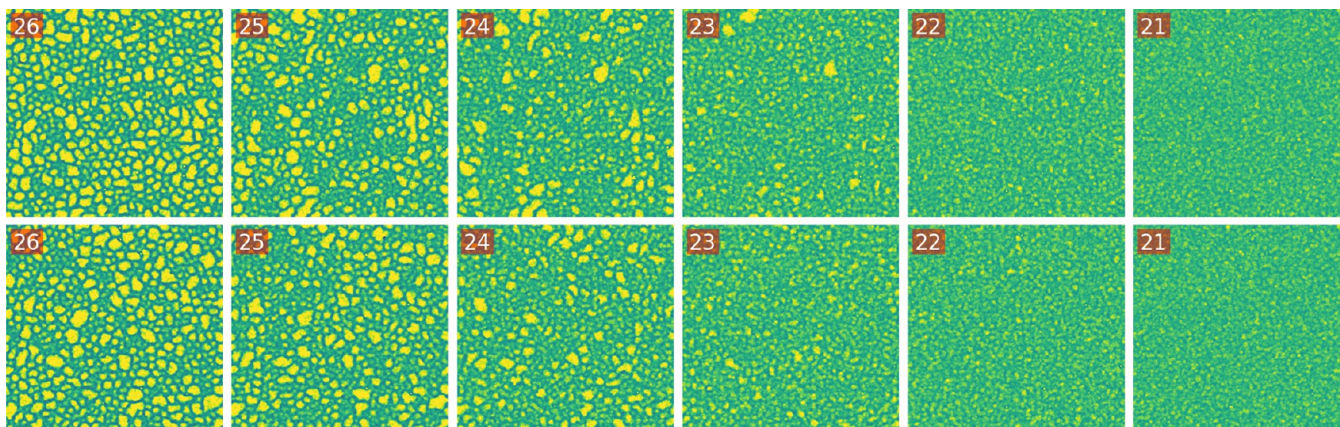


Figure 5. Instantaneous snapshots of the morphologies of the miktoarm polymer binary blend at $\phi_h = 0.4$ under thermal annealing. Top row: χN decreases from 26 (left) to 21 (right); the starting image of $\chi N = 26$ is obtained by performing a CL simulation for 10^5 steps initiated by random fields at $\chi N = 26$. Bottom row: χN increases from 21 (right) to 26 (left); the starting image of $\chi N = 21$ was obtained by a CL run for 5×10^4 steps initialized from a structureless disordered phase. All the subsequent images are obtained by running CL simulations for 5×10^4 steps initiated from the last configuration of the previous CL simulation. The size of each simulation cell is $110 \times 110 R_g$. The total density of A monomers is shown in each image.

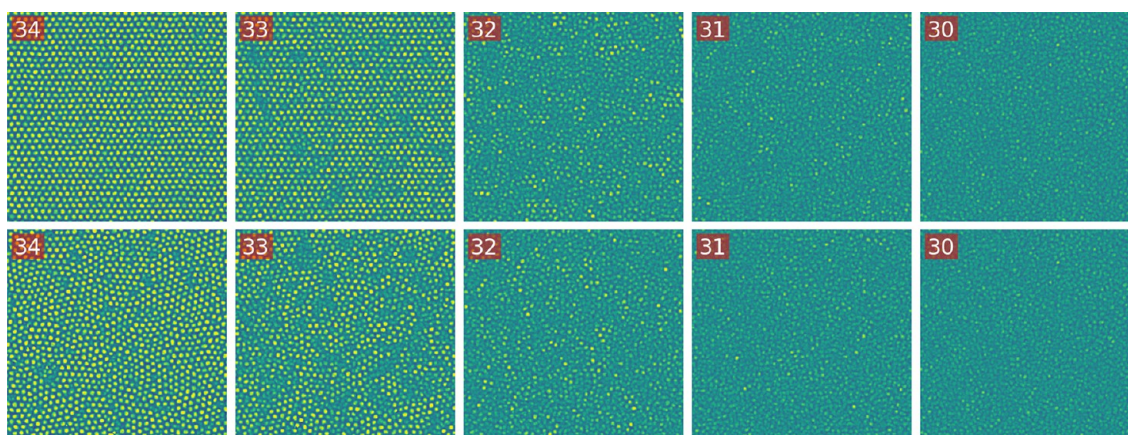


Figure 6. Instantaneous snapshots of the morphologies of the miktoarm polymer binary blend at $\phi_h = 0.1$ under thermal annealing. Top row: χN decreases from 34 (left) to 30 (right); the starting image of $\chi N = 34$ is obtained by performing a CL simulation for 10^5 steps initiated by HEX fields as calculated by SCFT at $\chi N = 34$. Bottom row: χN increases from 30 (right) to 34 (left); the starting image of $\chi N = 30$ was obtained from a CL simulation for 5×10^4 steps launched from a structureless disordered phase. All subsequent images are obtained by performing CL simulations for 5×10^4 steps initiated from the last configuration of the previous CL simulation. The size of each simulation cell is $111.8 \times 108.9 R_g$. The color bar is the same as in Figure 5.

domains until eventually macrophase separation occurs, followed by an inverted micellar phase.

Fluctuation-Corrected Phase Diagram. From our initial CL simulations it can be understood that the B&M mesophase is an equilibrium thermodynamic phase stabilized by thermal fluctuations. The mean-field phase diagram should be modified accordingly to accommodate the new phase. Here we locate phase boundaries by morphology characterization rather than detailed free-energy matching due to the computational expense of the latter.³⁸ We begin by conducting thermal annealing cycles by varying χN at fixed composition ϕ_h . Note that a decrease of χN corresponds to heating and an increase of χN corresponds to cooling. We subsequently employ isothermal blend composition sweeps by varying ϕ_h at fixed χN to efficiently localize phase boundaries that are almost vertical on χN – ϕ_h plots, such as those shown in Figure 2.

We initially vary χN with fixed $\phi_h = 0.4$. Two sequences of morphologies are presented in Figure 5: the top row shows a heating cycle (from left to right) while the bottom row shows cooling (from right to left), where each χN simulation begins

with the final field configuration from the previous. As χN decreases, the amplitude of the density of A monomers inside the A-rich domains gradually decreases accompanied by the reduction of the number of A-rich domains. During such a heating cycle, the B&M mesophase undergoes a gradual transition to the homogeneous DIS phase. The bottom row of Figure 5 shows that the B&M mesophase also emerges continuously from a homogeneous DIS phase during the cooling cycle. Furthermore, there is no significant hysteresis between the heating and cooling cycles, which signals that the transition between B&M and structureless DIS may be continuous. In fact, since the emerging B&M phase has the same translational and rotational symmetries (in the ensemble average) as the unstructured DIS phase, we conclude that they are one and the same and that no strict phase transition, even a continuous one, separates them. Nonetheless, it is useful to construct a “pseudo-phase-transition” boundary to approximately indicate where significant structure emerges in the disordered phase. For this particular case, the pseudotransition point is determined to be at approximately $\chi N = 22.5$ for $\phi_h = 0.4$ based on the criterion of the

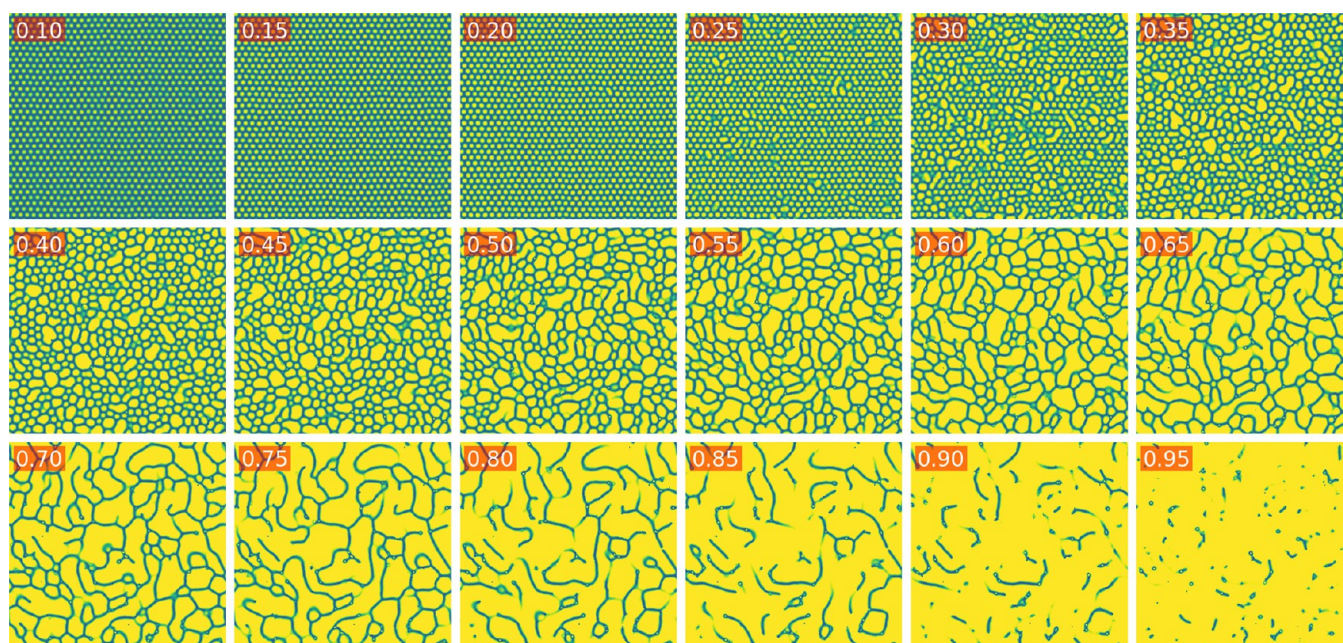


Figure 7. A sequence of CL morphologies of the miktoarm polymer binary blend from a composition sweep in ϕ_h at fixed $\chi N = 34$. ϕ_h increases from 0.1 to 0.95 in steps of 0.05 from left to right and top to bottom. The $\phi_h = 0.1$ simulation was initialized with an SCFT HEX phase and was run for 10^5 steps. All subsequent simulations were initiated from the last configuration of the previous simulation and were run for 5×10^4 steps. The size of each image is $111.8 \times 108.9 R_g$. The color bar is the same as Figure 5.

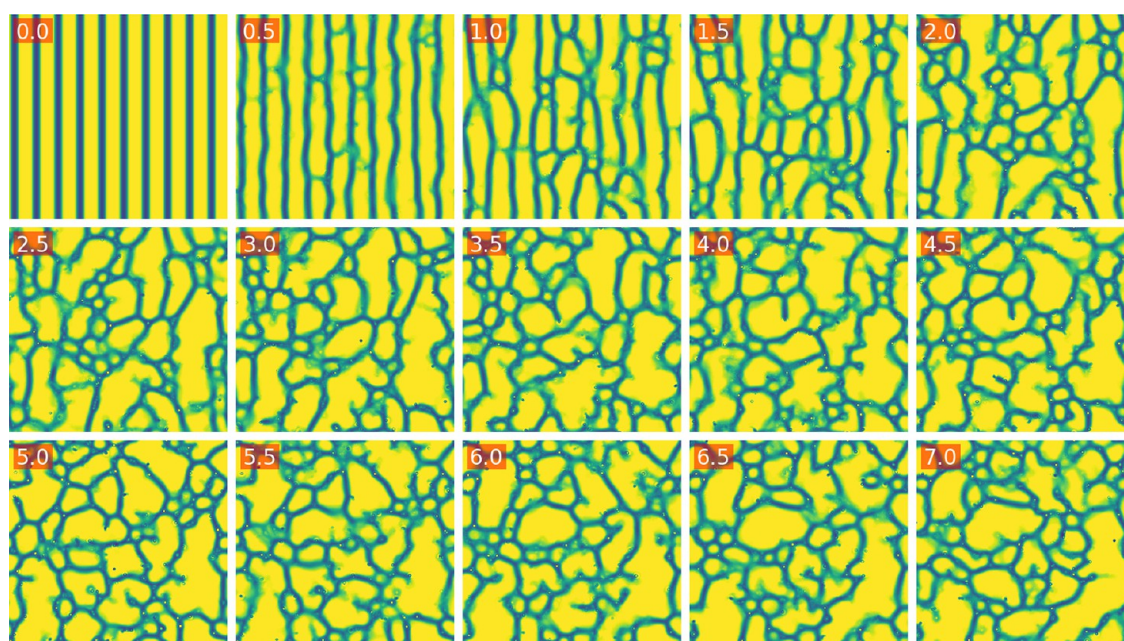


Figure 8. A sequence of morphologies of the miktoarm polymer binary blend for $\phi_h = 0.6$ and $\chi N = 34$ arising from CL simulations at increasing simulation time. The number in each image denotes the number of simulation steps in units of 1 million steps. The starting image is obtained by a SCFT calculation of a LAM morphology. The size of each image is $61.5 \times 61.5 R_g$. The color bar is the same as Figure 5.

disappearance of discrete A-rich domains during the heating cycle or the emergence of discrete A-rich domains during the cooling cycle. Using the same strategy, we have determined several transition points along the pseudo-DIS/B&M phase boundary, which are nearly coincident with the blue disorder to two-phase boundary in the SCFT phase diagram of Figure 2. Thus, thermal fluctuations destroy the DIS–DIS coexistence predicted by SCFT and instead gradually and continuously

introduce cellular nanostructure into the single DIS phase as χN is raised.

The transition between the HEX phase and the DIS phase is distinctly different from the formation of the B&M mesophase. Similar CL simulations have been performed for a binary blend with a lower homopolymer volume fraction ($\phi_h = 0.1$) and $\chi N = 34$, where the HEX phase is stable according to the mean-field theory (Figure 2). A sequence of morphologies from the heating and cooling cycle is presented in Figure 6. At such a low

homopolymer volume fraction, the B&M mesophase was not observed in our simulations. The heating cycle shown in the top row of Figure 6 indicates that the transition from the HEX phase to DIS is discontinuous, and a loss of long-range translational order occurs before the melting of A-rich domains.⁴ During the cooling cycle, a highly defective HEX morphology develops, as expected due to the accessible simulation time. The transition as such is identified as a discontinuous first-order order–disorder transition with accompanying hysteresis. HEX–DIS ODTs computed in this fashion are shown as blue points on Figure 9.

At the limit of very high homopolymer composition, CL simulations reveal a continuous evolution between micelles and a fluctuating DIS phase upon lowering χN . As with the case of the B&M to DIS transition, there is no symmetry change in transitioning between an unstructured DIS phase and a micellar DIS phase, so there can be no true phase transition. Nonetheless, we find that the blue macrophase boundary in the reference SCFT phase diagram of Figure 2 is again the approximation location where micelle-like structures begin to appear in CL simulations of the DIS phase.

For intermediate and strong segregation (i.e., $\chi N > 30$), phase boundaries are expected to vary less strongly with χN . In such cases it proves to be more convenient to locate order–order transitions by sweeping ϕ_h at fixed χN . One such isothermal blend–composition sweep is displayed in Figure 7. For small homopolymer volume fractions, the HEX phase is stable against thermal fluctuations. With increasing homopolymer content, the discrete A-rich domains coalesce into much larger, irregular domains with no apparent positional or orientational order. This coalescence eventually destroys the ordered HEX phase and leads to the formation of the B&M mesophase for $0.3 < \phi_h < 0.7$. Further increase of the homopolymer content causes the merging of swollen A-rich domains to percolation. Note that initially in this region most of B-rich domains are also still connected. We interpret this type of morphology as a macrophase separation of the B&M mesophase from an A-rich homogeneous phase, similar to experimental findings.⁵⁰ Finally, the B-rich domains become disconnected and break up into short worm-like micelles at even higher homopolymer volume fractions ($\phi_h > 0.8$). In short, we can identify three types of phase transitions: a transition from the HEX phase to the B&M mesophase, a transition to a macrophase coexistence of the B&M mesophase and a micellar phase, and finally a transition to a single micellar phase.

A potential difficulty in interpreting phase equilibria from the isothermal composition sweeps is that high symmetry phases, such as LAM, may not spontaneously re-form within accessible simulation times when transitioning from B&M. To demonstrate that LAM is indeed unstable to thermal fluctuations, as suggested by Figure 7, we conducted a long CL simulation initialized from a perfect LAM structure for a binary blend with $\phi_h = 0.6$ and $\chi N = 34$. A representative morphology evolution is shown in Figure 8. Here CL simulations with up to 7×10^6 steps were carried out to confirm that the orientational order inherited from the initial state of the LAM phase spontaneously disappears. For up to 2 million time steps, partial orientational ordering of the domains persists. However, given sufficient simulation time, all long-range positional and orientational order vanishes.

By combining these various CL results, we have constructed a proposed fluctuation-corrected phase diagram shown in Figure 9. In comparison with the reference SCFT phase diagram that is superimposed, we find that both ODTs and OOTs are substantially modified by thermal fluctuations. The region of

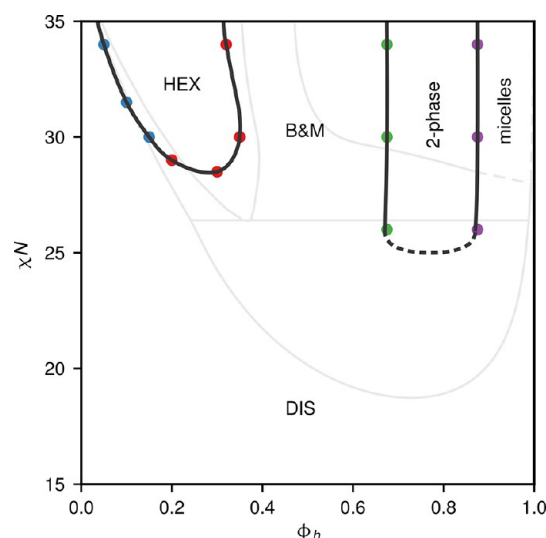


Figure 9. Complex Langevin fluctuation-corrected phase diagram of the miktoarm polymer binary blend. The dashed curve at the bottom of the two-phase region is hypothesized and has not been accurately calculated. The solid gray lines in the background are mean-field phase boundaries that are copied from Figure 2 for reference. The unstructured DIS phase transforms with χN continuously into either the B&M phase or the micellar phase, depending on blend composition, without any intervening phase transition.

HEX phase stability shrinks significantly compared to mean-field theory, especially at low χN or high ϕ_h , and the entire mean-field LAM region is replaced by the B&M mesophase, two-phase, and micelle regions. The mean-field two-phase regions, including the HEX/LAM coexistence and part of the DIS/DIS coexistence, are further consumed by the large fluctuation-induced B&M mesophase region. Note that the phase boundaries that enclose the B&M mesophase appear to be saturating at high χN , although the window of B&M stability is weakly expanding up to the largest segregation strengths explored here. We expect this trend will continue to the strong segregation regime, where the experiments were performed (the experimental interaction strength is estimated to be $\chi N \approx 270$).⁵⁰ The range of homopolymer volume fraction over which CL predicts the B&M mesophase to be stable agrees reasonably well with experimental observations, although the B&M mesophase was observed in the experiment for even lower homopolymer volume fraction than seen here ($0.1 \leq \phi_h \leq 0.3$). This minor discrepancy might be explained by the higher C or lower χN used in the CL simulations or by a long time scale for melting of HEX at lower ϕ_h that may have exceeded by the simulation times used. Finally, we should mention that the B&M mesophase observed in the CL simulations is clearly a structured phase lacking both positional and orientational order. In contrast, the B&M mesophase revealed by TEM in the experimental work shows evidence of layers and, hence, quasi long-range orientational order. One possible explanation is that the isotropic B&M mesophase observed in the simulations at weak to moderate segregation strength transforms to a “nematic” B&M mesophase at higher segregation strengths. This phase transition, if it exists, would likely be weak and first order in character.

CONCLUSIONS

In summary, we have performed a series of SCFT and CL simulations for various compositions and temperatures of a miktoarm star block copolymer/homopolymer binary blend, and

mean-field and fluctuation-corrected phase diagrams were constructed based on these simulations. The unconventional, aperiodic “bricks-and-mortar” mesophase, previously observed in experimental work, has been successfully reproduced by two-dimensional CL simulations for a wide range of homopolymer volume fractions and segregation strengths χN . It is found that no true phase transition separates the B&M mesophase and the homogeneous phase since transformation between the two is continuous and involves no detectable symmetry breaking or change of long-range positional and orientational order. For fixed χN and varying homopolymer volume fraction, the B&M mesophase appears in a channel between microphase separation (HEX) and macrophase separation. We have verified that ordered structures, specifically HEX and LAM, are unstable against thermal fluctuations and decay to B&M when placed inside the B&M mesophase region. Thus, our simulations reinforce the experimental finding that the B&M mesophase is a thermodynamic equilibrium phase.

It is important to emphasize that our CL simulations were all carried out in two-dimensional simulation cells, assuming homogeneity in the third dimension. Future work should confirm the stability of the B&M mesophase in 3D and illuminate its three-dimensional morphological nature. Moreover, we identified phase boundaries by a simple visual analysis of simulated morphologies. While we have taken care to test for stability and metastability through various annealing procedures, we cannot guarantee that the identified phase boundaries strictly map the equilibrium phase transitions. Delaney and Fredrickson³⁸ recently demonstrated an approach for generating complete fluctuation-corrected phase diagrams for block polymer melts. The method combines several advanced techniques, including the use of regularized models and field-theoretic thermodynamic integration for explicit Helmholtz free energy evaluation of each polymorph.⁴⁸ In principle, a similar approach could be used to map out the full phase diagram for this mikto polymer blend system, although the computational burden would be significant in the present case. Future methodological improvements notwithstanding, our current approach for mapping the B&M mesophase stability limits offers significant promise as a tool for molecular engineering. Specially, field-theoretic simulations with complex Langevin sampling can be used to explore broad architectural or compositional variations in mikto polymer alloys and to guide modification or improvement in the physical property profiles of these fascinating materials.

AUTHOR INFORMATION

Corresponding Author

*E-mail: ghf@mrl.ucsb.edu (G.H.F.).

ORCID

Yi-Xin Liu: 0000-0001-9374-5981

Notes

The authors declare no competing financial interest.

ACKNOWLEDGMENTS

Y.X.L. was supported by the China Scholarship Council (No. 201406105018). K.T.D. and G.H.F. were partially supported by the National Science Foundation under Award DMR-1506008 and by the Institute for Collaborative Biotechnologies through Grant W911NF-09-0001 from the U.S. Army Research Office. The content of the information presented here does not necessarily reflect the position or the policy of the U.S. Government, and no official endorsement shall be inferred.

Extensive use was made of the computational facilities of the UCSB Center for Scientific Computing at the CNSI and MRL: an NSF MRSEC (DMR-1121053) and NSF CNS-0960316.

ABBREVIATIONS

CL, complex Langevin; SCFT, self-consistent field theory; B&M, bricks and mortar; LAM, lamellae; HEX, hexagonal.

ADDITIONAL NOTE

“We note that the actual melting scenario is likely to be more complicated, involving an intermediate hexatic phase with quasi-long-range orientational order, due to the fact that the simulations were conducted in 2D.

REFERENCES

- (1) Matsen, M. W.; Schick, M. Stable and Unstable Phases of a Diblock Copolymer Melt. *Phys. Rev. Lett.* **1994**, *72*, 2660–2663.
- (2) Matsen, M. W. In *Soft Matter*; Gompper, G., Schick, M., Eds.; Wiley-VCH: Weinheim, 2006; Vol. 1, Chapter 2.
- (3) Bates, F. S.; Hillmyer, M. A.; Lodge, T. P.; Bates, C. M.; Delaney, K. T.; Fredrickson, G. H. Multiblock Polymers: Panacea or Pandora's Box? *Science* **2012**, *336*, 434–440.
- (4) Fredrickson, G. H. *The Equilibrium Theory of Inhomogeneous Polymers*; Clarendon Press: Oxford, 2006.
- (5) Arora, A.; Qin, J.; Morse, D. C.; Delaney, K. T.; Fredrickson, G. H.; Bates, F. S.; Dorfman, K. D. Broadly Accessible Self-Consistent Field Theory for Block Polymer Materials Discovery. *Macromolecules* **2016**, *49*, 4675–4690.
- (6) Mester, Z.; Lynd, N. A.; Fredrickson, G. H. Numerical Self-Consistent Field Theory of Multicomponent Polymer Blends in the Gibbs Ensemble. *Soft Matter* **2013**, *9*, 11288.
- (7) Drolet, F.; Fredrickson, G. H. Combinatorial Screening of Complex Block Copolymer Assembly with Self-Consistent Field Theory. *Phys. Rev. Lett.* **1999**, *83*, 4317–4320.
- (8) Matsen, M. W. Effect of Architecture on the Phase Behavior of AB-Type Block Copolymer Melts. *Macromolecules* **2012**, *45*, 2161–2165.
- (9) Matsen, M. W. Gyroid versus Double-Diamond in ABC Triblock Copolymer Melts. *J. Chem. Phys.* **1998**, *108*, 785–796.
- (10) Matsen, M. W. Stabilizing New Morphologies by Blending Homopolymer with Block Copolymer. *Phys. Rev. Lett.* **1995**, *74*, 4225–4228.
- (11) Tyler, C.; Morse, D. C. Orthorhombic Fddd Network in Triblock and Diblock Copolymer Melts. *Phys. Rev. Lett.* **2005**, *94*, 208302.
- (12) Gao, Y.; Deng, H.; Li, W.; Qiu, F.; Shi, A. C. Formation of Nonclassical Ordered Phases of AB-Type Multiarm Block Copolymers. *Phys. Rev. Lett.* **2016**, *116*, 068304.
- (13) Liu, M.; Qiang, Y.; Li, W.; Qiu, F.; Shi, A. C. Stabilizing the Frank-Kasper Phases via Binary Blends of AB Diblock Copolymers. *ACS Macro Lett.* **2016**, *5*, 1167–1171.
- (14) Xie, N.; Li, W.; Qiu, F.; Shi, A. C. σ Phase Formed in Conformationally Asymmetric AB-Type Block Copolymers. *ACS Macro Lett.* **2014**, *3*, 906–910.
- (15) Xie, N.; Liu, M.; Deng, H.; Li, W.; Qiu, F.; Shi, A. C. Macromolecular Metallurgy of Binary Mesocrystals via Designed Multiblock Terpolymers. *J. Am. Chem. Soc.* **2014**, *136*, 2974–2977.
- (16) Müller, M.; Schmid, F. Incorporating Fluctuations and Dynamics in Self-Consistent Field Theories for Polymer Blends. *Adv. Polym. Sci.* **2005**, *185*, 1–58.
- (17) Khandpur, A. K.; Forster, S.; Bates, F. S.; Hamley, I. W.; Ryan, A. J.; Bras, W.; Almdal, K.; Mortensen, K. Diblock Copolymer Phase Diagram near the Order-Disorder Transition. *Macromolecules* **1995**, *28*, 8796–8806.
- (18) Fredrickson, G. H.; Helfand, E. Fluctuation Effects in the Theory of Microphase Separation in Block Copolymers. *J. Chem. Phys.* **1987**, *87*, 697–705.

- (19) Bates, F. S.; Rosedale, J. H.; Fredrickson, G. H.; Glinka, C. J. Fluctuation-Induced First-Order Transition of an Isotropic System to a Periodic State. *Phys. Rev. Lett.* **1988**, *61*, 2229–2232.
- (20) Bates, F.; Maurer, W.; Lipic, P.; Hillmyer, M.; Almdal, K.; Mortensen, K.; Fredrickson, G.; Lodge, T. Polymeric Bicontinuous Microemulsions. *Phys. Rev. Lett.* **1997**, *79*, 849–852.
- (21) Hillmyer, M. A.; Maurer, W. W.; Lodge, T. P.; Bates, F. S.; Almdal, K. Model Bicontinuous Microemulsions in Ternary Homopolymer/Block Copolymer Blends. *J. Phys. Chem. B* **1999**, *103*, 4814–4824.
- (22) Washburn, N. R.; Lodge, T. P.; Bates, F. S. Ternary Polymer Blends as Model Surfactant Systems. *J. Phys. Chem. B* **2000**, *104*, 6987–6997.
- (23) Müller, M.; Schick, M. Bulk and Interfacial Thermodynamics of a Symmetric, Ternary Homopolymer-Copolymer Mixture: a Monte Carlo Study. *J. Chem. Phys.* **1996**, *105*, 8885–8901.
- (24) Kielhorn, L.; Muthukumar, M. Spinodal Decomposition of Symmetric Diblock Copolymer/Homopolymer Blends at the Lifshitz Point. *J. Chem. Phys.* **1999**, *110*, 4079–4089.
- (25) Fredrickson, G. H.; Bates, F. S. Design of Bicontinuous Polymeric Microemulsions. *J. Polym. Sci., Part B: Polym. Phys.* **1997**, *35*, 2775–2786.
- (26) Fredrickson, G. H.; Bates, F. S. Stabilizing Co-continuous Polymer Blend Morphologies with ABC Block Copolymers. *Eur. Phys. J. B* **1998**, *1*, 71–76.
- (27) Liang, H.; He, X.; Jiang, W.; Jiang, B. Monte Carlo Simulation of Phase Separation of A/B/A-B Ternary Mixtures. *Macromol. Theory Simul.* **1999**, *8*, 173–178.
- (28) Werner, A.; Schmid, F.; Muller, M. Monte Carlo Simulations of Copolymers at Homopolymer Interfaces: Interfacial Structure as a Function of the Copolymer Density. *J. Chem. Phys.* **1999**, *110*, 5370–5379.
- (29) Matsen, M. W. Elastic Properties of a Diblock Copolymer Monolayer and Their Relevance to Bicontinuous Microemulsion. *J. Chem. Phys.* **1999**, *110*, 4658–4667.
- (30) Poncela, A.; Rubio, A. M.; Freire, J. J. Gibbs Ensemble Simulation of Symmetric Mixtures Composed by the Homopolymers AA, BB and Their Common Block Copolymer AB. *J. Chem. Phys.* **2003**, *118*, 425–433.
- (31) Düchs, D.; Ganesan, V.; Fredrickson, G. H.; Schmid, F. Fluctuation Effects in Ternary AB+A+B Polymeric Emulsions. *Macromolecules* **2003**, *36*, 9237–9248.
- (32) Klauder, J. R.; Lee, S. Improved Complex Langevin Method for (2 + 1)-Dimensional Lattices. *Phys. Rev. D: Part. Fields* **1992**, *45*, 2101–2104.
- (33) Parisi, G. On Complex Probabilities. *Phys. Lett. B* **1983**, *131*, 393–395.
- (34) Ganesan, V.; Fredrickson, G. H. Field-Theoretic Polymer Simulations. *Europhys. Lett.* **2001**, *55*, 814–820.
- (35) Fredrickson, G. H.; Ganesan, V.; Drolet, F. Field-Theoretic Computer Simulation Methods for Polymers and Complex Fluids. *Macromolecules* **2002**, *35*, 16–39.
- (36) Alexander-Katz, A.; Moreira, A. G.; Fredrickson, G. H. Field-Theoretic Simulations of Confined Polymer Solutions. *J. Chem. Phys.* **2003**, *118*, 9030–9036.
- (37) Alexander-Katz, A.; Moreira, A. G.; Sides, S. W.; Fredrickson, G. H. Field-Theoretic Simulations of Polymer Solutions: Finite-size and Discretization Effects. *J. Chem. Phys.* **2005**, *122*, 014904.
- (38) Delaney, K. T.; Fredrickson, G. H. Recent Developments in Fully Fluctuating Field-Theoretic Simulations of Polymer Melts and Solutions. *J. Phys. Chem. B* **2016**, *120*, 7615–7634.
- (39) Koski, J.; Chao, H.; Riggleman, R. A. Field Theoretic Simulations of Polymer Nanocomposites. *J. Chem. Phys.* **2013**, *139*, 244911.
- (40) Chao, H.; Hagberg, B. A.; Riggleman, R. A. The Distribution of Homogeneously Grafted Nanoparticles in Polymer Thin Films and Blends. *Soft Matter* **2014**, *10*, 8083–8094.
- (41) Popov, Y. O.; Lee, J.; Fredrickson, G. H. Field-Theoretic Simulations of Polyelectrolyte Complexation. *J. Polym. Sci., Part B: Polym. Phys.* **2007**, *45*, 3223–3230.
- (42) Lee, J.; Popov, Y. O.; Fredrickson, G. H. Complex Coacervation: A Field Theoretic Simulation Study of Polyelectrolyte Complexation. *J. Chem. Phys.* **2008**, *128*, 224908.
- (43) Riggleman, R. A.; Kumar, R.; Fredrickson, G. H. Investigation of the Interfacial Tension of Complex Coacervates using Field-Theoretic Simulations. *J. Chem. Phys.* **2012**, *136*, 024903.
- (44) Lennon, E. M.; Mohler, G. O.; Cenicerros, H. D.; García-Cervera, C. J.; Fredrickson, G. H. Numerical Solutions of the Complex Langevin Equations in Polymer Field Theory. *Multiscale Model. Simul.* **2008**, *6*, 1347–1370.
- (45) Delaney, K. T.; Fredrickson, G. H. Polymer Field-Theory Simulations on Graphics Processing Units. *Comput. Phys. Commun.* **2013**, *184*, 2102–2110.
- (46) Villet, M. C.; Fredrickson, G. H. Efficient Field-Theoretic Simulation of Polymer Solutions. *J. Chem. Phys.* **2014**, *141*, 224115.
- (47) Düchs, D.; Delaney, K. T.; Fredrickson, G. H. A Multi-species Exchange Model for Fully Fluctuating Polymer Field Theory Simulations. *J. Chem. Phys.* **2014**, *141*, 174103.
- (48) Lennon, E. M.; Katsov, K.; Fredrickson, G. H. Free Energy Evaluation in Field-Theoretic Polymer Simulations. *Phys. Rev. Lett.* **2008**, *101*, 138302.
- (49) Riggleman, R. A.; Fredrickson, G. H. Field-Theoretic Simulations in the Gibbs Ensemble. *J. Chem. Phys.* **2010**, *132*, 024104.
- (50) Shi, W.; Hamilton, A. L.; Delaney, K. T.; Fredrickson, G. H.; Kramer, E. J.; Ntaras, C.; Avgeropoulos, A.; Lynd, N. A.; Demassieux, Q.; Creton, C. Aperiodic “Bricks and Mortar” Mesophase: A New Equilibrium State of Soft Matter and Application as A Stiff Thermoplastic Elastomer. *Macromolecules* **2015**, *48*, 5378–5384.
- (51) Lynd, N. A.; Oyerokun, F. T.; O'Donoghue, D. L.; Handlin, D. L.; Fredrickson, G. H. Design of Soft and Strong Thermoplastic Elastomers Based on Nonlinear Block Copolymer Architectures Using Self-Consistent-Field Theory. *Macromolecules* **2010**, *43*, 3479–3486.
- (52) Wang, Z. G. Fluctuation in Electrolyte Solutions: The Self Energy. *Phys. Rev. E* **2010**, *81*, 021501.
- (53) Cenicerros, H. D.; Fredrickson, G. H. Numerical Solution of Polymer Self-Consistent Field Theory. *Multiscale Model. Simul.* **2004**, *2*, 452–474.
- (54) Rasmussen, K.; Kalosakas, G. Improved Numerical Algorithm for Exploring Block Copolymer Mesophases. *J. Polym. Sci., Part B: Polym. Phys.* **2002**, *40*, 1777–1783.
- (55) Tzeremes, G.; Rasmussen, K.; Lookman, T.; Saxena, A. Efficient Computation of the Structural Phase Behavior of Block Copolymers. *Phys. Rev. E: Stat. Phys., Plasmas, Fluids, Relat. Interdiscip. Top.* **2002**, *65*, 041806.
- (56) Matsen, M. W. Phase Behavior of Block Copolymer/Homopolymer Blends. *Macromolecules* **1995**, *28*, 5765–5773.
- (57) Matsen, M. W. Equilibrium Behavior of Asymmetric ABA Triblock Copolymer Melts. *J. Chem. Phys.* **2000**, *113*, 5539–5544.
- (58) Knoll, K.; Niessner, N. Styrolux and Styroflex - From Transparent High Impact Polystyrene to New Thermoplastic Elastomers. *Macromol. Symp.* **1998**, *132*, 231–243.